Assessing volcanic hazard at Campi Flegrei caldera (Italy) with uncertainty quantification

Andrea Bevilacqua[1, 2], Augusto Neri[1], Tomaso Esposti Ongaro[1], Roberto Isaia[3], Willy Aspinall[4], Peter J. Baxter[5], Antonella Bertagnini[1], Marina Bisson[1], Franco Flandoli[6], Enrico Iannuzzi[3], Marco Pistolesi[7], Simone Orsucci[1], Mauro Rosi[8, 9] and Stefano Vitale[10]

(1) Istituto Nazionale di Geofisica e Vulcanologia, Sezione di Pisa, Pisa, Italy
(2) Scuola Normale Superiore, Pisa, Italy
(3) Istituto Nazionale di Geofisica e Vulcanologia, Osservatorio Vesuviano, Napoli, Italy
(4) University of Bristol, School of Earth Sciences, Bristol, and Aspinall and Associates, Tisbury, United Kingdom
(5) University of Cambridge, Institute of Public Health, Cambridge, United Kingdom
(6) Università di Pisa, Dip.to di Matematica, Pisa, Italy
(7) Università di Firenze, Dip.to di Scienze della Terra, Firenze, Italy
(8) Università di Pisa, Dip.to di Scienze della Terra, Pisa, Italy
(9) Dip.to della Protezione Civile, Roma, Italy
(10) Università di Napoli Federico II, Dip.to di Scienze della Terra, dell'Ambiente e delle Risorse, Napoli, Italy

Science, uncertainty and decision making in the mitigation of natural risks
Dipartimento della Protezione Civile, 8-10 October 2014

Cost Action IS1304
Expert Judgement Network: Bridging the Gap Between Scientific Uncertainty and Evidence-Based Decision Making

cost
EUROPEAN COOPERATION IN SCIENCE AND TECHNOLOGY

EUROPEAN SCIENCE FOUNDATION

The objective

Campi Flegrei is an active volcanic area situated in the Campanian Plain (Italy) and formed by a resurgent caldera with a diameter of about 12 km and more than three hundred thousand people living inside it. Pyroclastic density currents (PDCs) are common and very dangerous phenomena.

PDC hazard mapping in the Campi Flegrei caldera is particularly challenging due to:

- the large uncertainty on **future vent location**;
- the unpredictable **scale of future activity**;
- the **complex dynamics of PDC.**

A **quantitative probabilistic mapping of PDC invasion**, possibly able to account for the main **intrinsic uncertainties** of the system, is needed for hazard assessment.

We focused our work on the **quantification of some of the different sources of uncertainty** in order to produce median and quantile probabilistic maps.

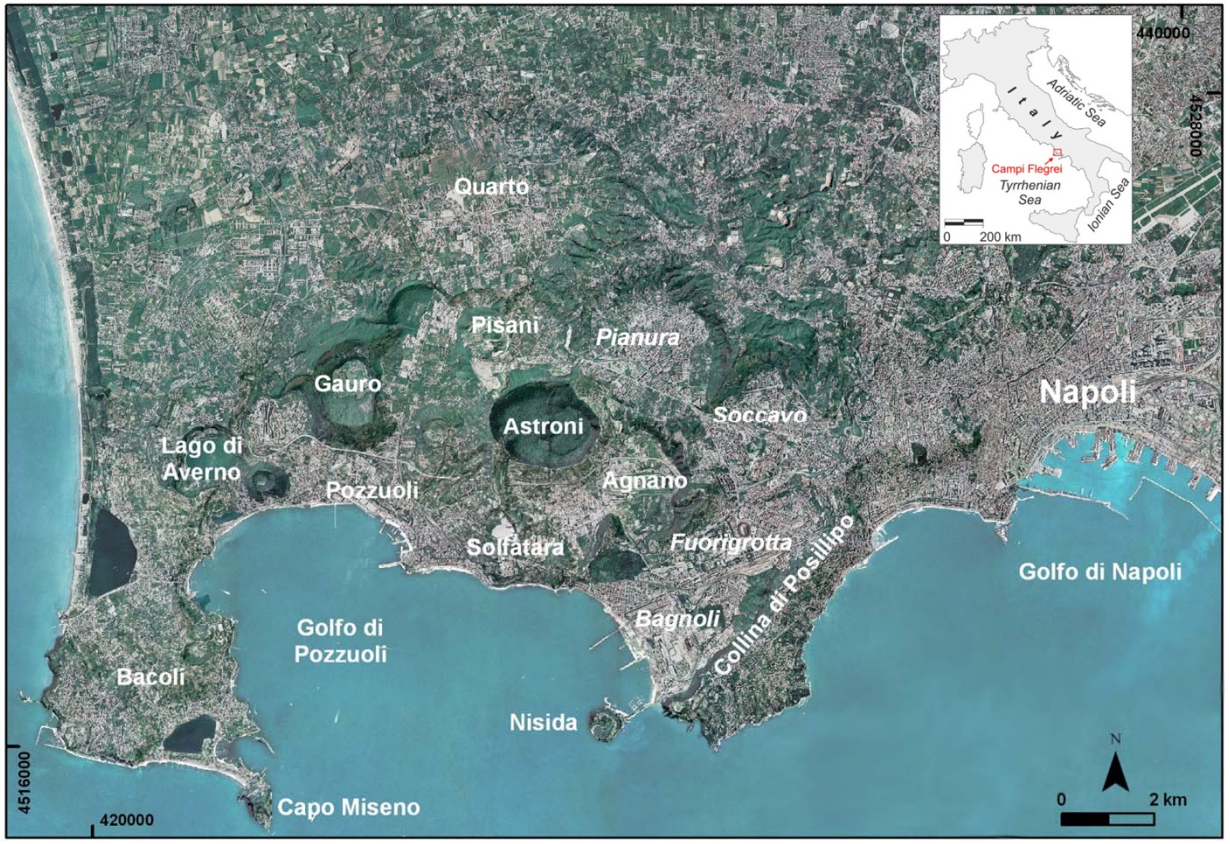

Figure 1. Mosaic of orthophotos of Campi Flegrei caldera and surrounding areas (including the city of Naples on the west) showing the large urbanization inside and around this active volcano [Bisson et al., 2007].

The methodology – Phase I: Vent opening map

Our methodology is based on the assumption that the probability of new vent opening can be computed as a **weighted linear combination** of the spatial distributions of key variables of the system that reflect, or can influence, this volcanic process.

A key aspect of the study was the ***identification***, and where possible the ***quantification***, of **some of the main sources of epistemic uncertainty** that are associated with the available data and therefore need to be reflected in the final maps.
In particular, these are:

- the **uncertainty on location** of past eruptive vents;

- the number of past events which do not correspond to presently identified vents but which do exist in the stratigraphic evidences (so-called "***lost vents***");

- the **uncertainty of linear weights** to be associated with the variables that contribute to the definition of the mapping

Vent opening data with uncertainty

Large ellipses mostly indicate lack of constraints and **large uncertainty** in the locality of the vent.

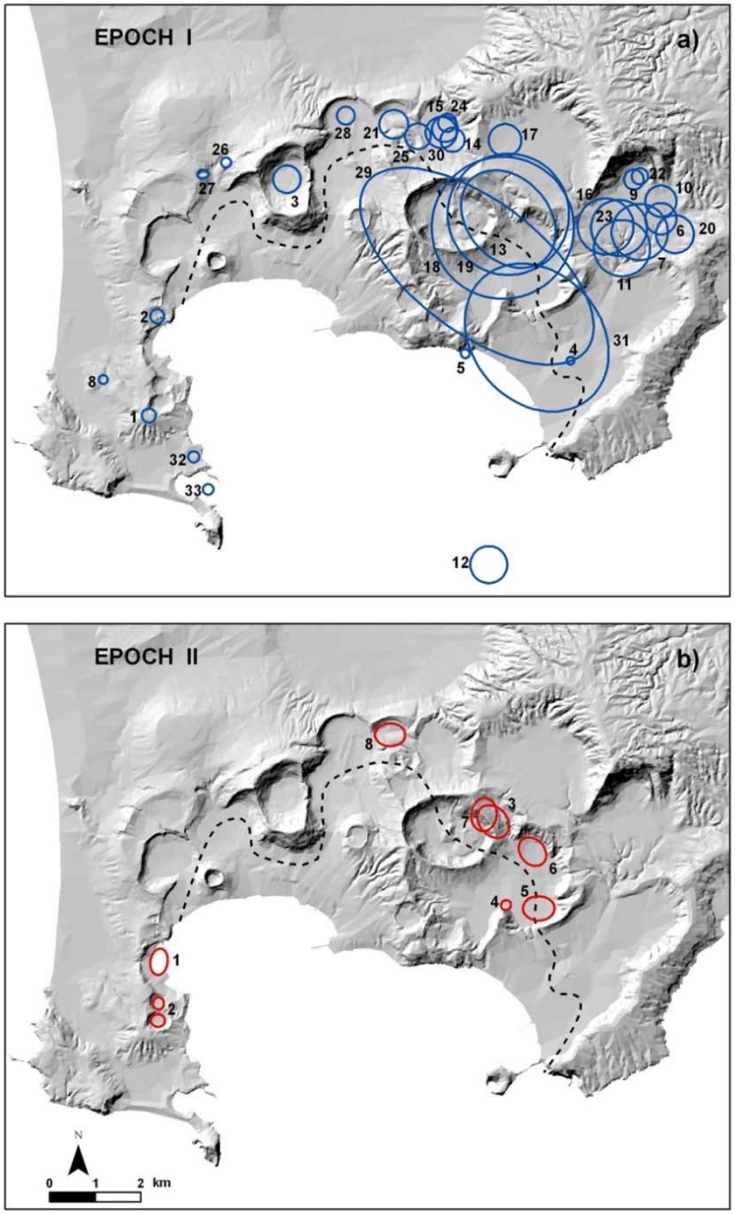

ID	Eruptive Vent - Ep. I
1	Bellavista
2	Mofete
3	Gauro
4	Santa Teresa
5	La Pietra
6	La Pigna 1
7	La Pigna 2
8	Torre Cappella
9	Minopoli 1
10	Paradiso
11	Soccavo 1
12	Gaiola
13	Pomici Principali
14	Paleo Pisani 1
15	Paleo Pisani 2
16	Soccavo 2
17	Soccavo 3
18	S4s3_1
19	S4s3_2
20	Soccavo 4
21	Paleo San Martino
22	Minopoli 2
23	Soccavo 5
24	Pisani 1
25	Pisani 2
26	Fondo Riccio
27	Concola
28	Montagna Spaccata
29	Pignatiello 1
30	Pisani 3
31	Casale
32	Bacoli
33	Porto Miseno

ID	Eruptive Vent - Ep. II
1	Baia
2	Fondi di Baia
3	Sartania 1
4	Monte Spina Lava Dome
5	Costa San Domenico
6	Pigna San Nicola
7	Sartania 2
8	San Martino

Vent location uncertainty

Epoch I

Epoch II

Coastline

Epoch I - II

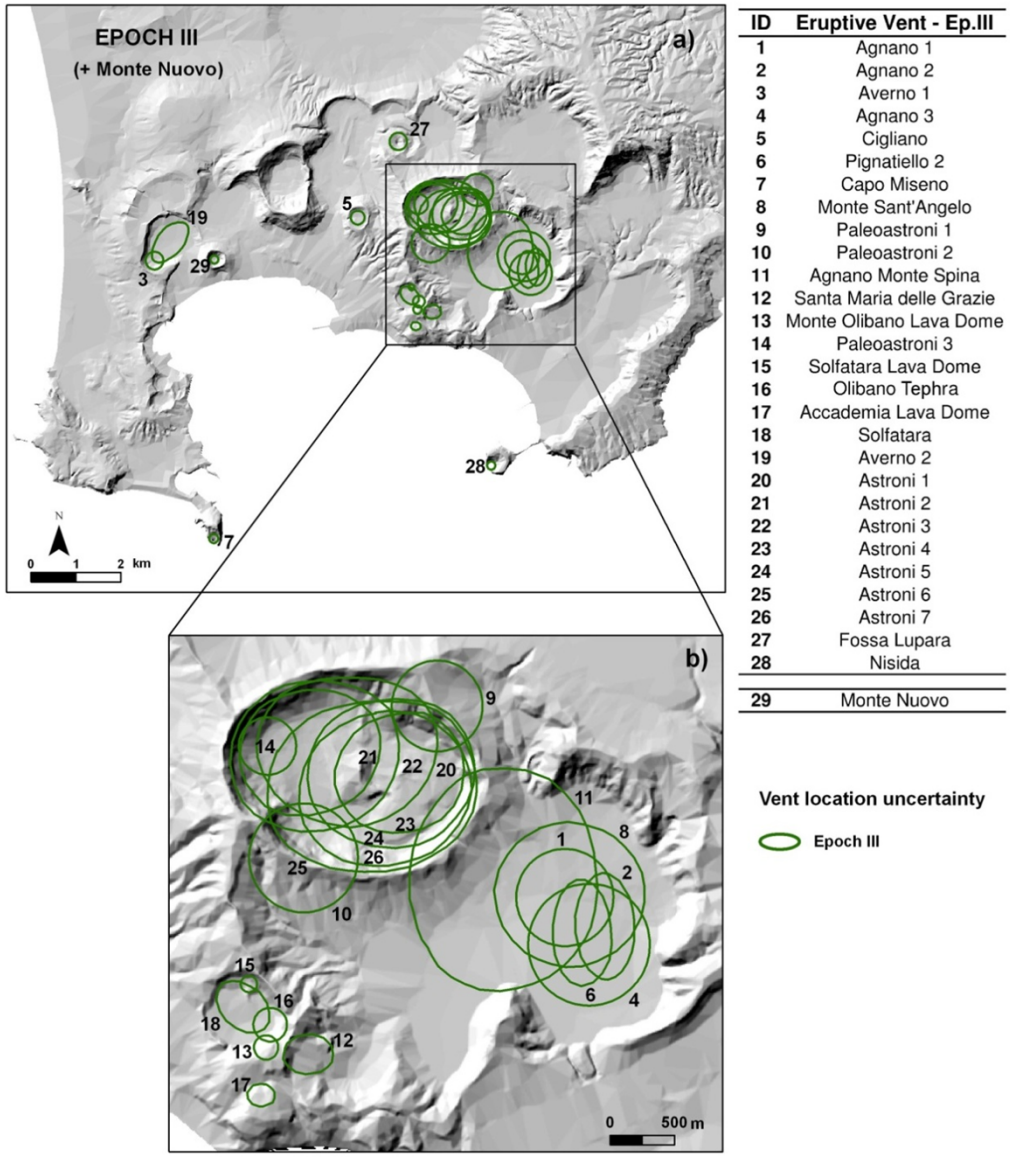

ID	Eruptive Vent - Ep.III
1	Agnano 1
2	Agnano 2
3	Averno 1
4	Agnano 3
5	Cigliano
6	Pignatiello 2
7	Capo Miseno
8	Monte Sant'Angelo
9	Paleoastroni 1
10	Paleoastroni 2
11	Agnano Monte Spina
12	Santa Maria delle Grazie
13	Monte Olibano Lava Dome
14	Paleoastroni 3
15	Solfatara Lava Dome
16	Olibano Tephra
17	Accademia Lava Dome
18	Solfatara
19	Averno 2
20	Astroni 1
21	Astroni 2
22	Astroni 3
23	Astroni 4
24	Astroni 5
25	Astroni 6
26	Astroni 7
27	Fossa Lupara
28	Nisida
29	Monte Nuovo

Vent location uncertainty

Epoch III

Figure 2. Reconstruction of the location of the **eruptive vents and fissures** for the events occurred in (a) Epoch I (15 – 10.6 kyr) and Epoch II (9.6 – 9.1 kyr), (b) Epoch III (5.5 – 3.8 kyr) and of the Monte Nuovo eruption (1538 AD). Numbered circles and ellipses indicate the **assumed vent location** of the events listed on the right side of the maps. The name of the events follows Smith et al. [2011] and Isaia et al. [2014].

Vent opening probability maps based on past vents

We adopted **two different approaches** that produced quite consistent results.

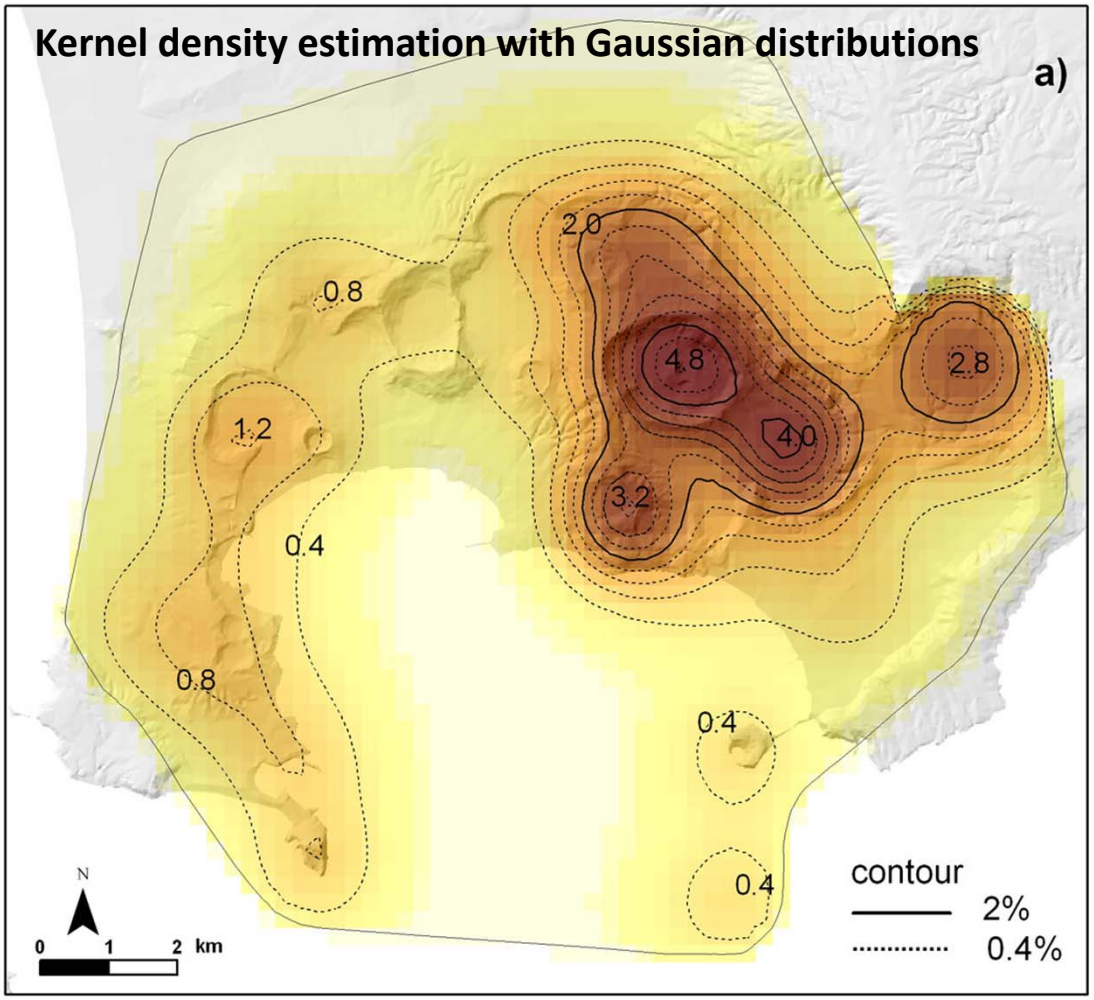

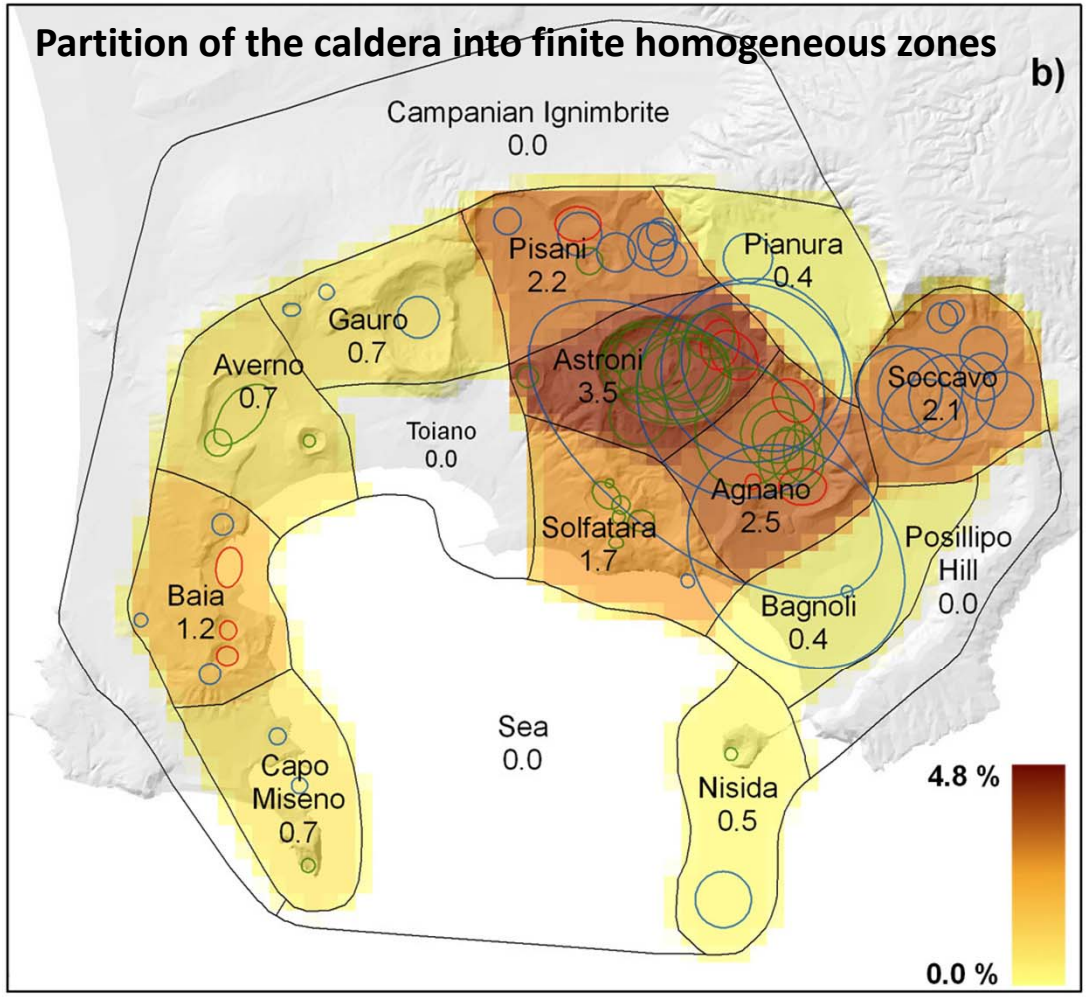

Figure 3. (a) Density distribution of the probability of vent opening obtained by using the vent location data of the three epochs of activity reported in Figures 3 and a **kernel density estimation**. Contour and colour values indicate the percentage probability of vent opening per km^2 (conditioned to the occurrence of an eruption).

(b) Density distribution of the probability of vent opening obtained by using the vent location data of the three epochs of activity reported in Figures 3 and the **partitioning of the caldera** in 16 homogeneous zones. Values reported in the different sub-areas indicate the percentage probability of vent opening per km^2 (conditioned to the occurrence of an eruption). Both the representations assume to give the same weight to the information from each epoch of activity.

Vent opening probability maps based on faults and fractures

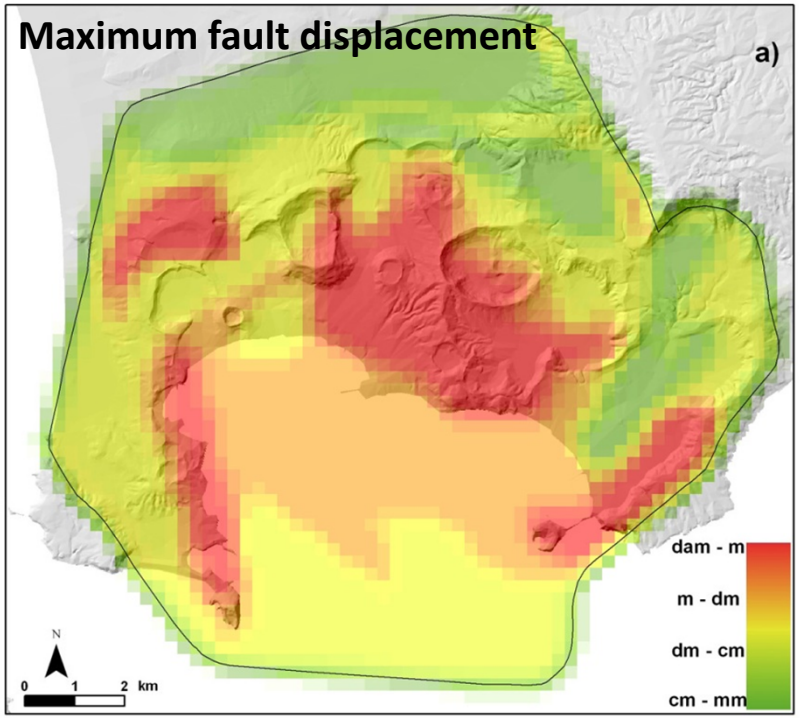

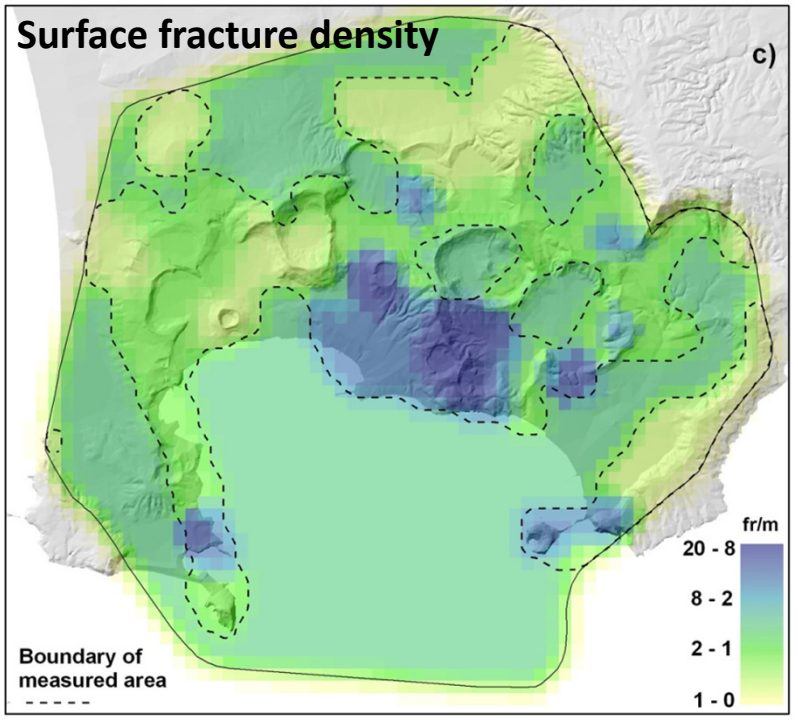

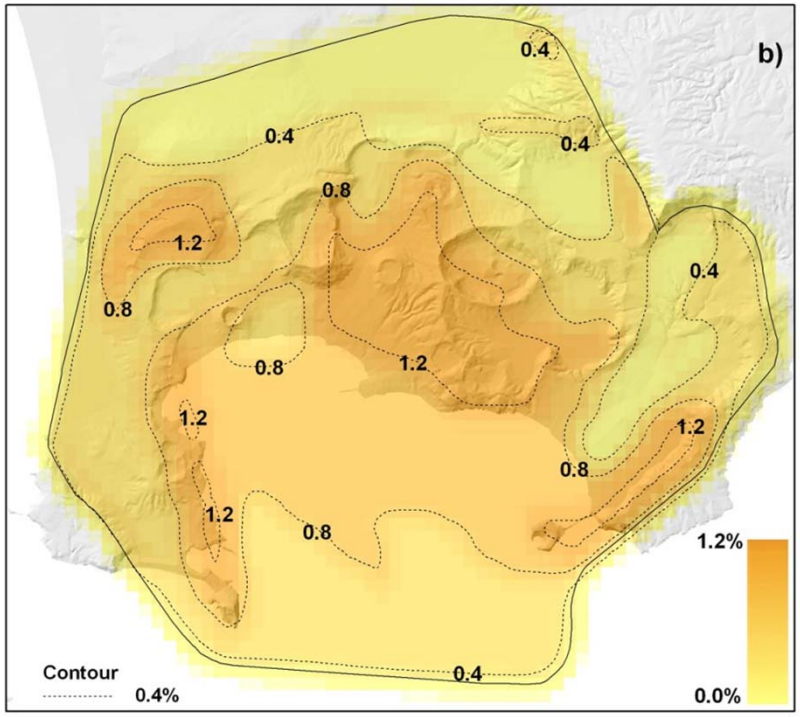

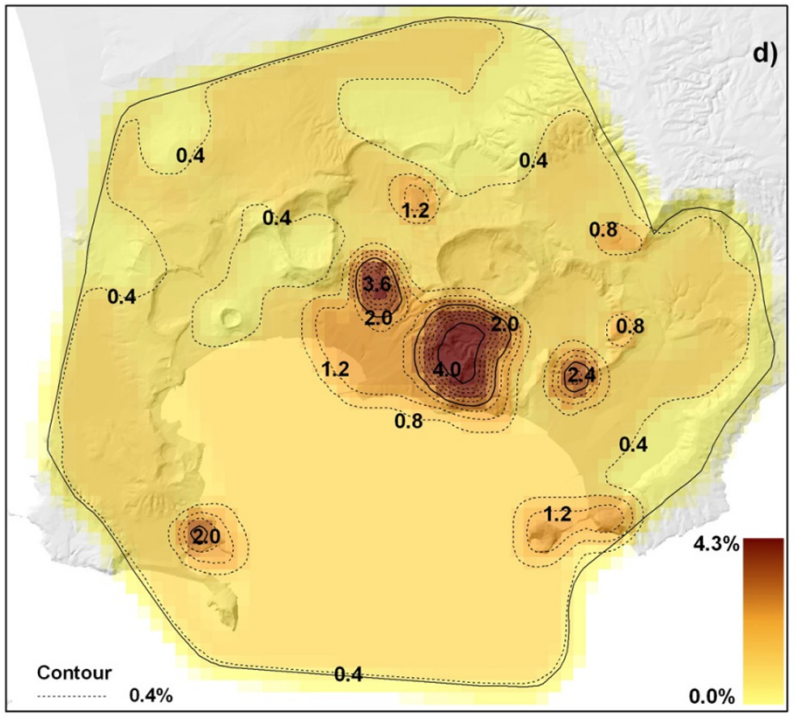

Figure 4. (a) Distribution of the **maximum fault displacement** in the caldera as derived from the dataset of Vitale and Isaia [2014]. The four colour levels shown correspond to displacements of different **orders of magnitude** ranging from sub-centimetric to metric scales.

(c) Distribution of the **surface fracture density** in the caldera as derived from the dataset of Vitale and Isaia (2014). In this case the four colours correspond to different **values of density** ranging between about 1 and 20 fractures per meter (fr/m). Wide areas of the inland caldera and the offshore part were not measured. In these areas the **average value** of the total measured zone was assumed.

(b-d) Density distribution of the probability of vent opening obtained **normalizing** the values of maximum fault displacement and of surface fracture density (percentage probability of vent opening per km^2 conditioned to the occurrence of an eruption).

Assignment of weights by expert judgement

We followed a **structured elicitation procedure** aimed at acquiring and understanding the experts' opinions about uncertainty quantification for the factors considered.

Several elicitation sessions, involving **8 experts** with different volcanological backgrounds (all included as authors of this study), were carried out during the two-years long study through several **meetings** and also email consultations.

The seed questions were about carefully researched aspects of Campi Flegrei volcanism, other Italian volcanoes, such as Vesuvius, and about explosive volcanism in general.

For each question (seed or target), each expert expressed his views as the values of the 5^{th}, 50^{th} and 95^{th} percentiles of **simple uncertainty profiles**.

We computed three different **Decision Makers (DM)** using three different methods:

- the **Cooke Classical Model (CM)** (Cooke, 1991), which score is based on the two empirically determined measures, *calibration* and *information* (with an optimization step);

- a complementary approach, i.e. the **Expected Relative Frequency model (ERF)** [Flandoli et al., 2011], which score can be interpreted as the *expected accuracy* of the expert.

- an **Equal Weights pooling (EW)** of the experts' uncertainty densities;

The hierarchical logic tree

To simplify the quantification of the weight to assign to each spatial distribution, we defined a **simple hierarchical logic tree**.

Most of the **target questions** that were asked quantify the **relative importance**, or relevance, of one variable or feature of the system versus others.

The DM percentiles values were used to define **triangular distributions**, from which randomized sample values could be generated for each question. We followed a **Monte Carlo simulation approach** for determining the single branch weight estimates, normalizing complementary values to sum to one, and then **multiplying the single weights over each branch** of the logic tree.

Beside the other relevant maps, we assumed a uniform **homogenous map** over the NYT caldera to represent the possible lack of information.

Other relevant questions were about the estimation of the **number of 'lost vents'** in each epoch of activity, assumed uniform on the inland portion of the caldera.

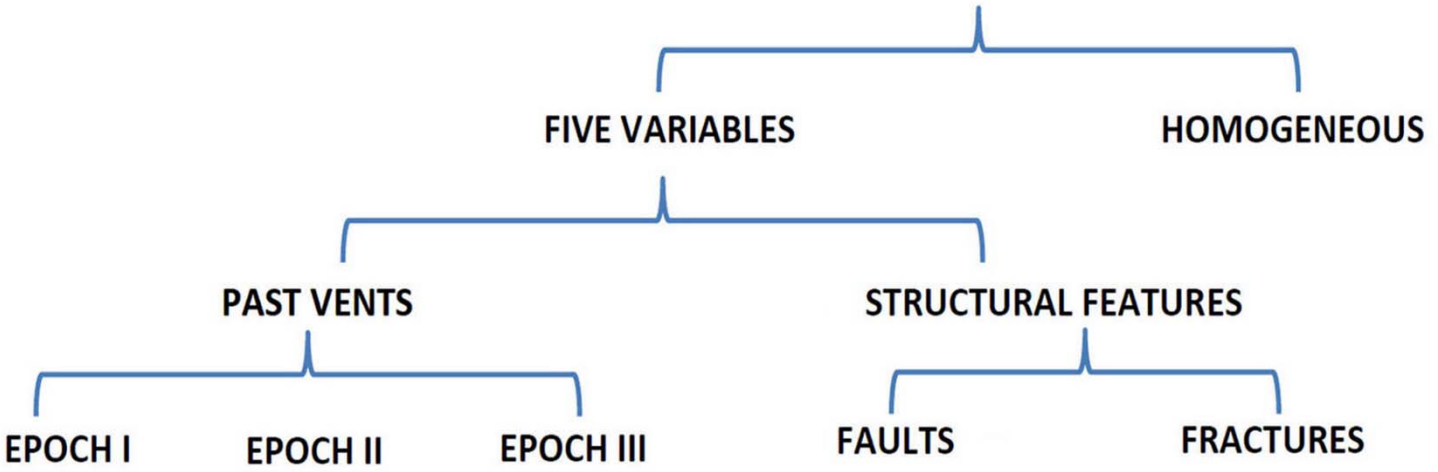

Figure 5. Hierarchical logic tree structure associated to the target questions queried during the elicitation sessions.

Weights estimation

Variable/ Percentiles	Vents Epoch I	Vents Epoch II	Vents Epoch III	Lost vents	Faults	Fractures	Homog. map
5%ile	6.3 9.5 6.3	1.3 2.2 1.5	10.2 14.7 7.6	3.3 4.2 3.4	8.1 10.2 5.3	5.4 7.0 4.3	6.3 8.7 6.5
Mean	16.0 16.4 17.7	4.5 4.8 4.6	20.4 22.5 19.3	5.9 6.3 6.7	16.4 16.5 13.8	11.9 12.3 12.0	24.9 21.3 25.9
95%ile	26.7 24.0 30.5	8.7 7.6 9.3	33.3 31.6 33.8	9.0 8.8 11.0	26.6 23.9 24.3	20.4 18.6 22.0	42.4 31.1 45.4

Table 1. Probability percentages of the mean and 5th and 95th **percentiles of the weight** of the five variables considered together with the weights of the lost vents and homogeneous map.

The three values reported in each cell refer to, from top to bottom, **the CM, ERF and EW models**. The median values (i.e. the 50th percentile) are very similar to the mean values within about 1%.

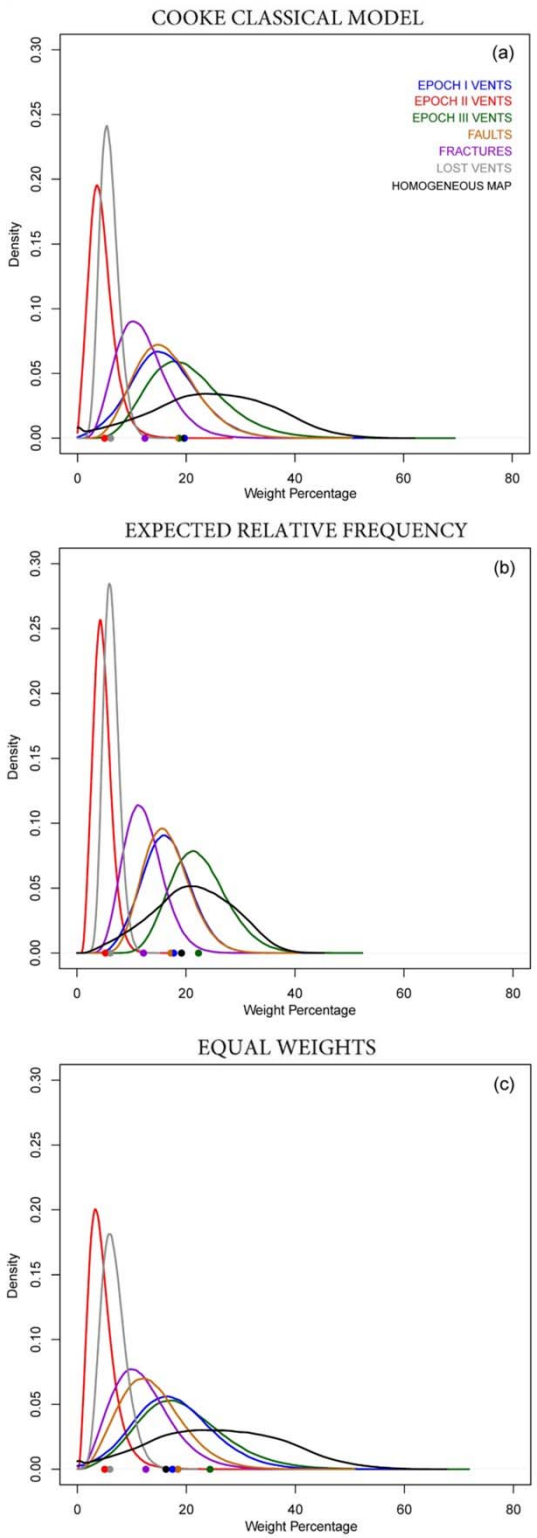

Figure 6. **Density distribution of the weights** of the six variables considered and of the lost vents as a function of the elicitation models assumed, i.e. (a) Cooke CM, (b) ERF model and (c) EW model. Along the x axis are also reported as coloured dots the estimates obtained by using just the **best-guess** (central) values provided by the experts.

Vent opening probability maps

Kernel density estimation

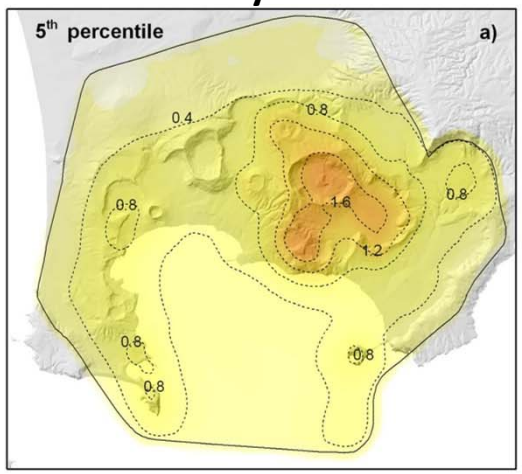

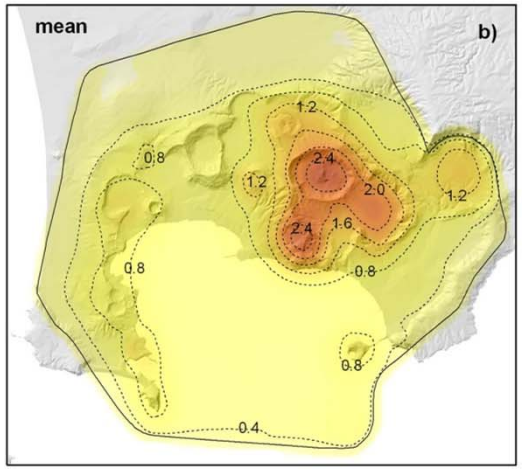

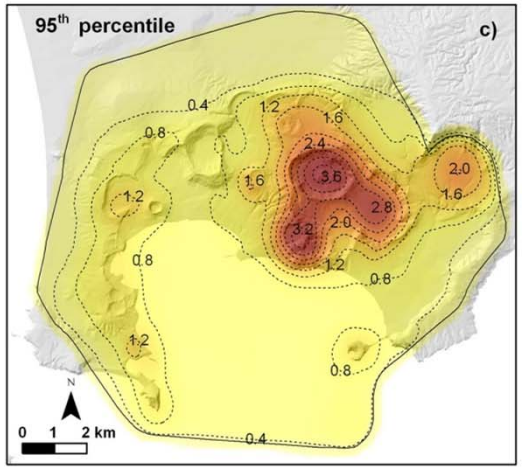

Partition of the caldera

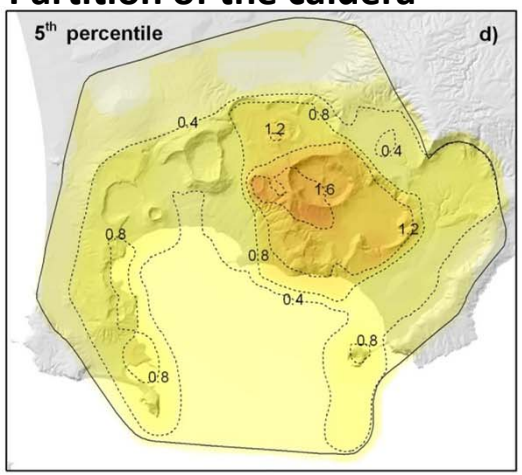

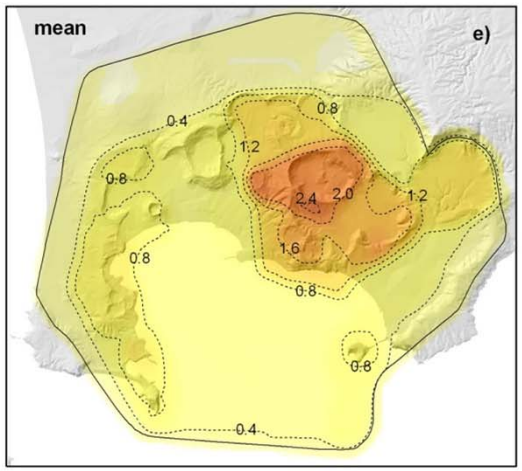

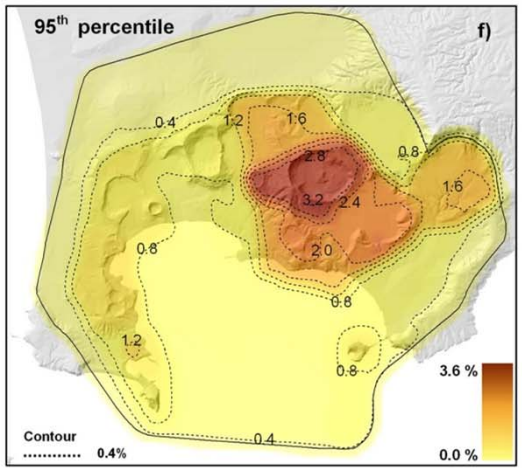

Results have shown evidence for a main **high probability** region in the **central-eastern portion of the caldera**.

Significantly lower **secondary largest** are found to exist in both the **eastern and western parts of the caldera**.

Nevertheless the spatial distribution of vent opening position **probability is widely dispersed** over the whole NYT caldera, including the offshore portion.

We accompany our probabilities with **quantified uncertainty estimates** which are indicative, typically, of spreads ±30% on the local mean value.

Figure 7. Probability maps of new vent opening as obtained weighting the six variable distributions considered. Contours and colours indicate the probability of vent opening per km2 (conditioned to the occurrence of an eruption).

(a), (b) and (c) refer to the use of **kernel functions** for the estimate of the density of past vents, whereas (d), (e) and (f) refer to the **partition of the caldera** in the 16 homogeneous zones. Maps (a) and (d) refer to the 5th percentile, (b) and (e) to the mean values and (c) and (f) to the 95th percentile. The median maps result very similar to the corresponding mean maps.

The methodology – Phase II. PDC invasion probability

The next slides focus on the definition of **quantitative probabilistic PDC invasion hazard maps** for the CF area, incorporating key controlling, but uncertain, variables of the system, particularly **vent location** and **eruptive scale** of future activity.

We produced probabilistic maps by a nested **Monte Carlo simulation** approach, using a **simplified PDC invasion model** able to represent main topographic effects.

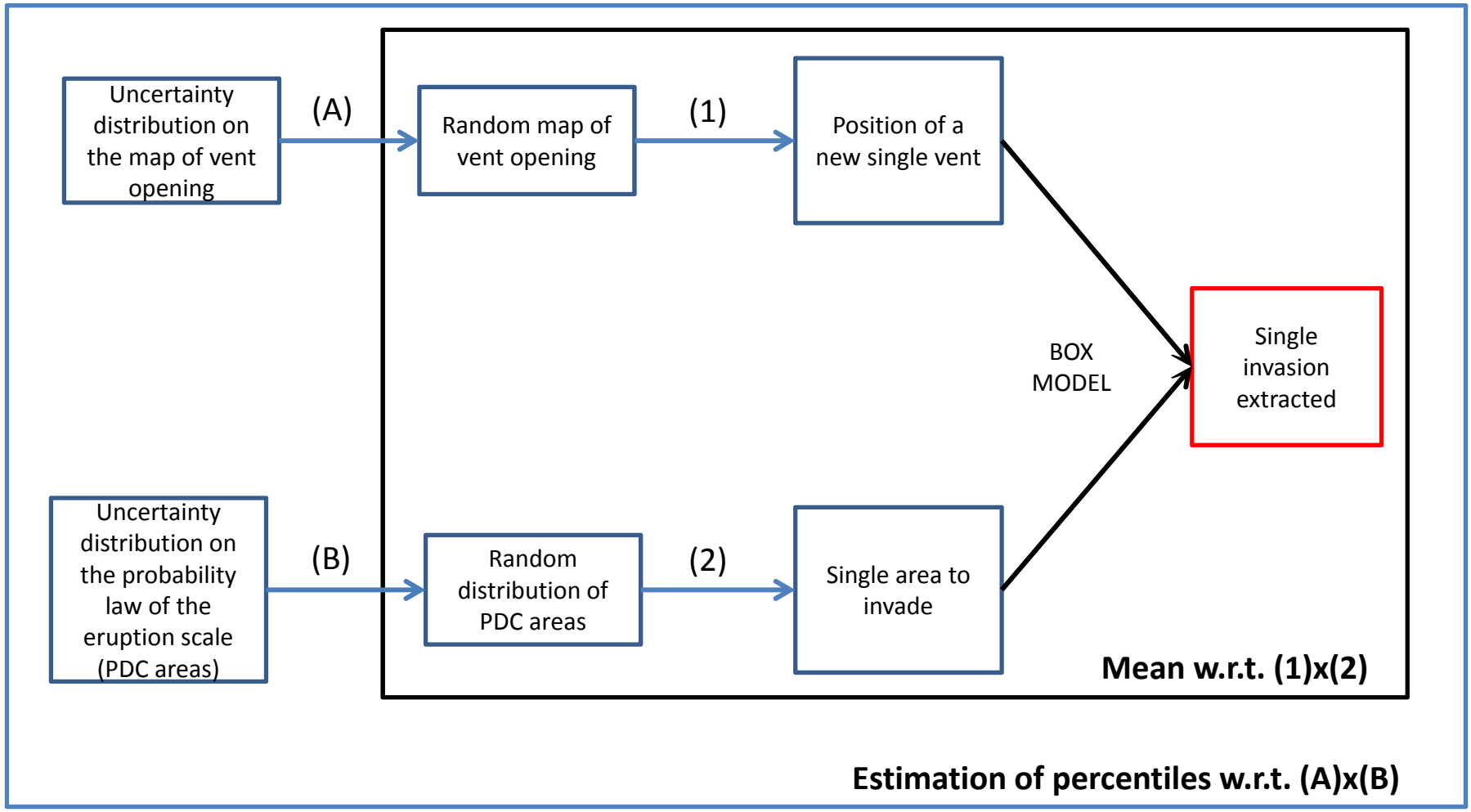

Figure 8. Scheme of the **nested Monte Carlo simulation** producing the probability maps of PDC invasion; each arrow represent a random draw.

The reconstructed PDC invasion areas

In the analysis, we designated the **areas invaded by the PDCs** as a variable representative of the distribution of the PDC scale. Data were mostly based on the work of Orsi et al. (2004).

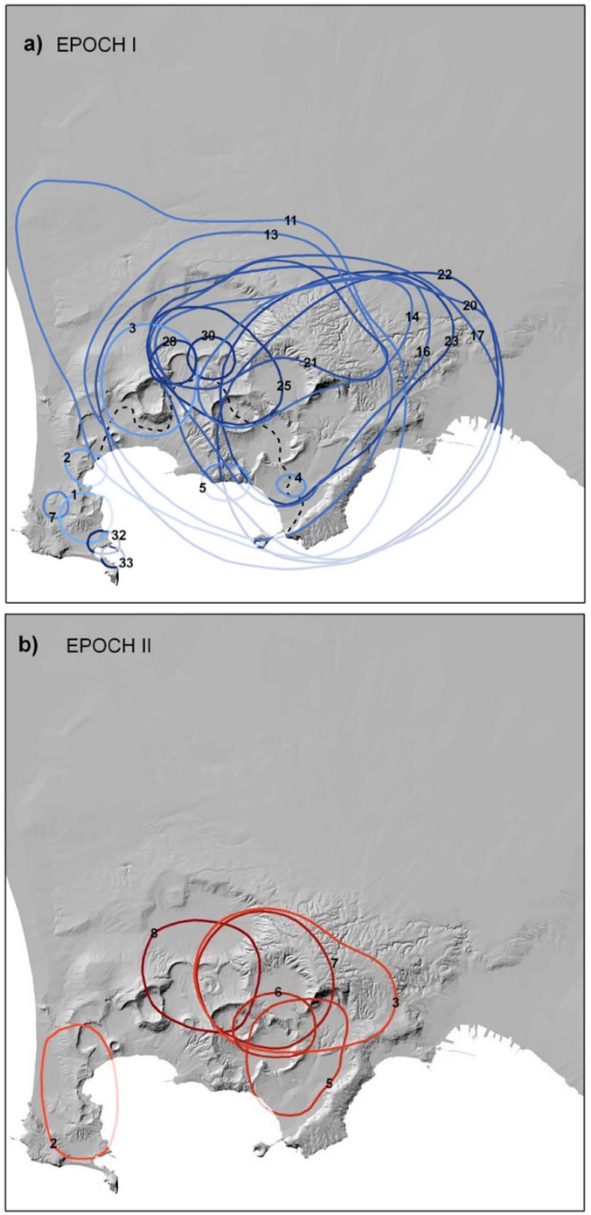

ID	PDC Deposit - Epoch I	Area (km^2)
1	Bellavista Volcano	3.9
2	Mofete Volcano	2.1
3	Gauro Volcano	16.1
4	Santa Teresa Volcano	0.9
5	La Pietra Volcano	2.6
7	Torre Cappella Volcano	1.0
11	Soccavo 1 Tephra	190.5
13	Pomici Principali Tephra	129.2
14	Paleo Pisani 2 Tephra	37.7
16	Soccavo 2 Tephra	75.8
17	Soccavo 3 Tephra	147.5
20	Soccavo 4 Tephra	180.2
21	Paleo San Martino Tephra	37.3
22	Minopoli 2 Tephra	113.6
23	Soccavo 5 Tephra	66.2
25	Pisani 2 Tephra	21.1
28	Montagna Spaccata Tephra	3.0
30	Pisani 3 Tephra	3.0
32	Bacoli Volcano	1.1
33	Porto Miseno Volcano	0.7

ID	PDC Deposit - Epoch II	Area (km^2)
2	Fondi di Baia Tephra	15.7
3	Sartania 1 Tephra	40.7
5	Costa San Domenico Tephra	16.9
6	Pigna San Nicola Tephra	8.0
7	Sartania 2 Tephra	27.0
8	San Martino Tephra	19.7

ID	PDC Deposit - Epoch III	Area (km^2)
2	Agnano 2 Tephra	17.1
3	Averno 1 Tephra	27.0
4	Agnano 3 Tephra	68.0
5	Cigliano Tephra	28.3
7	Capo Miseno Volcano	1.1
8	Monte Sant'Angelo Tephra	43.8
9	Paleoastroni 1 Tephra	18.1
10	Paleoastroni 2 Tephra	5.4
11	Agnano Monte Spina Tephra	312.5
18	Solfatara Tephra	8.7
19	Averno 2 Tephra	24.8
20	Astroni 1 Tephra	39.7
21	Astroni 2 Tephra	19.1
22	Astroni 3 Tephra	41.1
23	Astroni 4 Tephra	60.4
24	Astroni 5 Tephra	29.1
25	Astroni 6 Tephra	26.9
26	Astroni 7 Tephra	10.2
27	Fossa Lupara Tephra	8.9
28	Nisida Tephra	4.7
29	Monte Nuovo Tephra	5.7

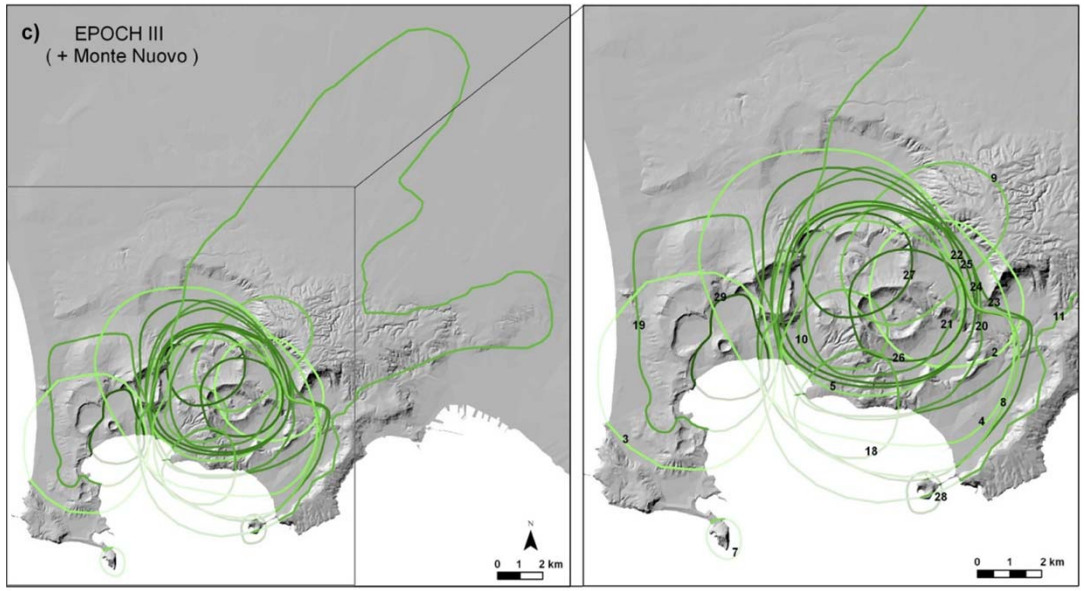

Figure 9. Reconstruction of the **distribution of PDC deposits** generated by explosive events that occurred in: (a) Epoch I, (b) Epoch II, and (c) Epoch III plus the Monte Nuovo event. Numbers refer to the events reported in the legend.

Reported deposit boundaries were **extended over the sea** to allow estimation of reasonable values for PDC invasion area (shown in the legend). Data were derived and updated from Orsi et al. [2004]. The distribution shown for the AMS PDCs was derived from de Vita et al. [1999]. Naming of events follows Smith et al. [2011].

Probability law of the distribution of PDC invasion areas

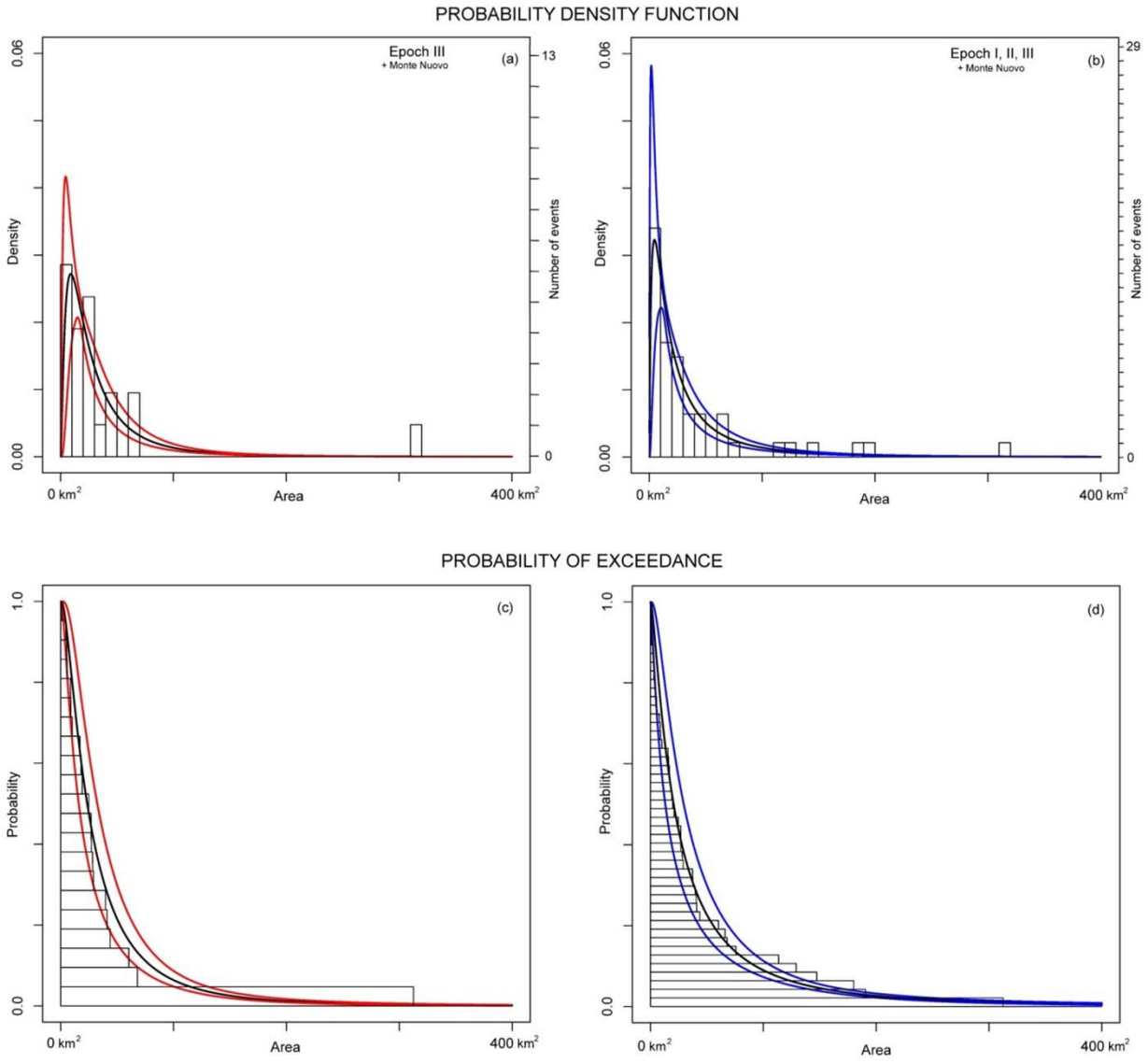

The **radial underestimation** error of deposit boundaries, as shown in Figure 9, was considered to vary between about 150 and 1,000 m, with a mean value of about 500 m

In addition, we added **the lost PDC invasion areas** up to 10 and 50 km2, randomly extrapolated following the distribution obtained from the known invasion areas.

Figure 10. Histograms of the PDC invasion areas as estimated from Figure 9 for: (a) Epoch III and (b) all three Epochs (plus the Monte Nuovo event in both cases).

(a) and (b) also show probability **density functions** for the invasion areas after consideration of underestimations of PDC run-out and the addition of 'lost deposits'.

(c) and (d) show probability **exceedance curves** (survival functions) corresponding to the two periods considered, 5kyr and 15 kyr.

The curves relate to the 5th, 50th and 95th percentiles of such uncertainty sources and to a **Maximum Likelihood (ML) lognormal distribution**, although other distributions were also considered.

The propagation model of PDC based on energy decay

$$\begin{cases} u = \dfrac{dl}{dt} = Fr(g_p \phi h)^{1/2}, \\ \dfrac{d\phi}{dt} = -w_s \dfrac{\phi}{h}, \\ l^2 h = V. \end{cases}$$

Our integral model allows computation of **flow kinematics** and the **maximum distance** (flow run-out) reached over a sub-horizontal surface by a current generated by instantaneous release of a finite volume of gas and solid particles.

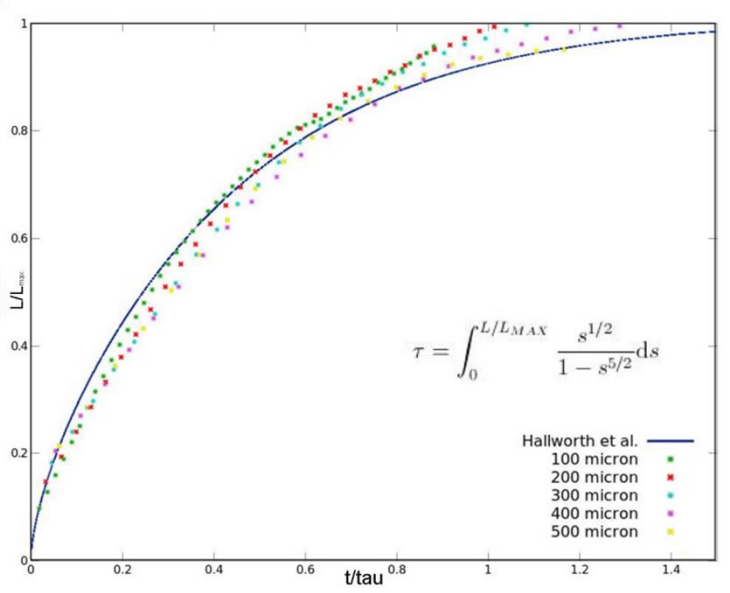

Figure 11. Non-dimensional front position versus non-dimensional time for particle-laden currents with different values of the Sauter particle diameter. (2D numerical simulation)

In order to quantify **main effects of topography** on the propagation of a PDC, the **flow kinetic energy** was compared to the **potential energy required** to overcome the topographical reliefs that the flow encounters.

In this study the PDC invasion model was applied in an **inverse mode**, i.e. starting from the **estimate of the invaded area** obtained using the density functions described before and then computing the **volume required** to generate such propagation, given a specific vent location and surrounding topography.

$$C = (Fr^2 w_s \phi_0 g_p)^{1/3} / 2$$

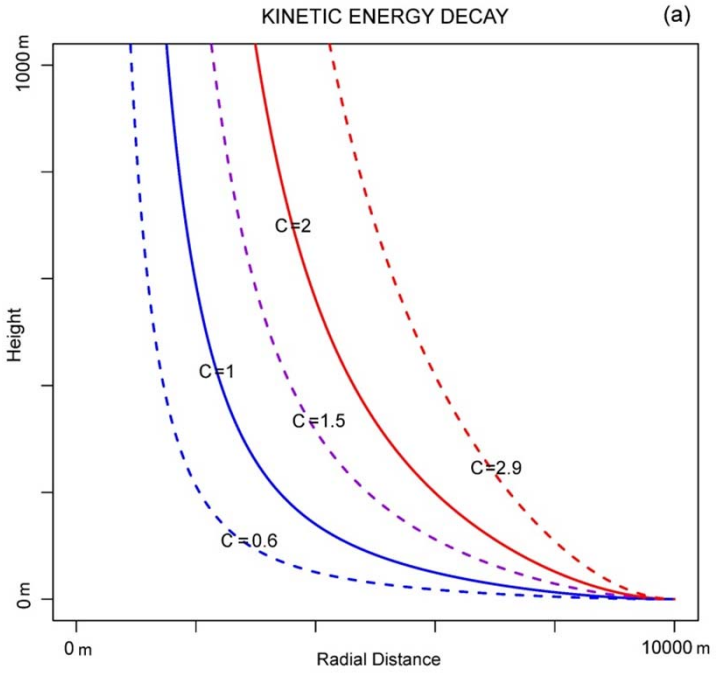

Figure 12. Example of decay of flow head kinetic energy expressed in terms of potential height as a function of distance from the source. Curves refer to a flow run-out of 10 km.

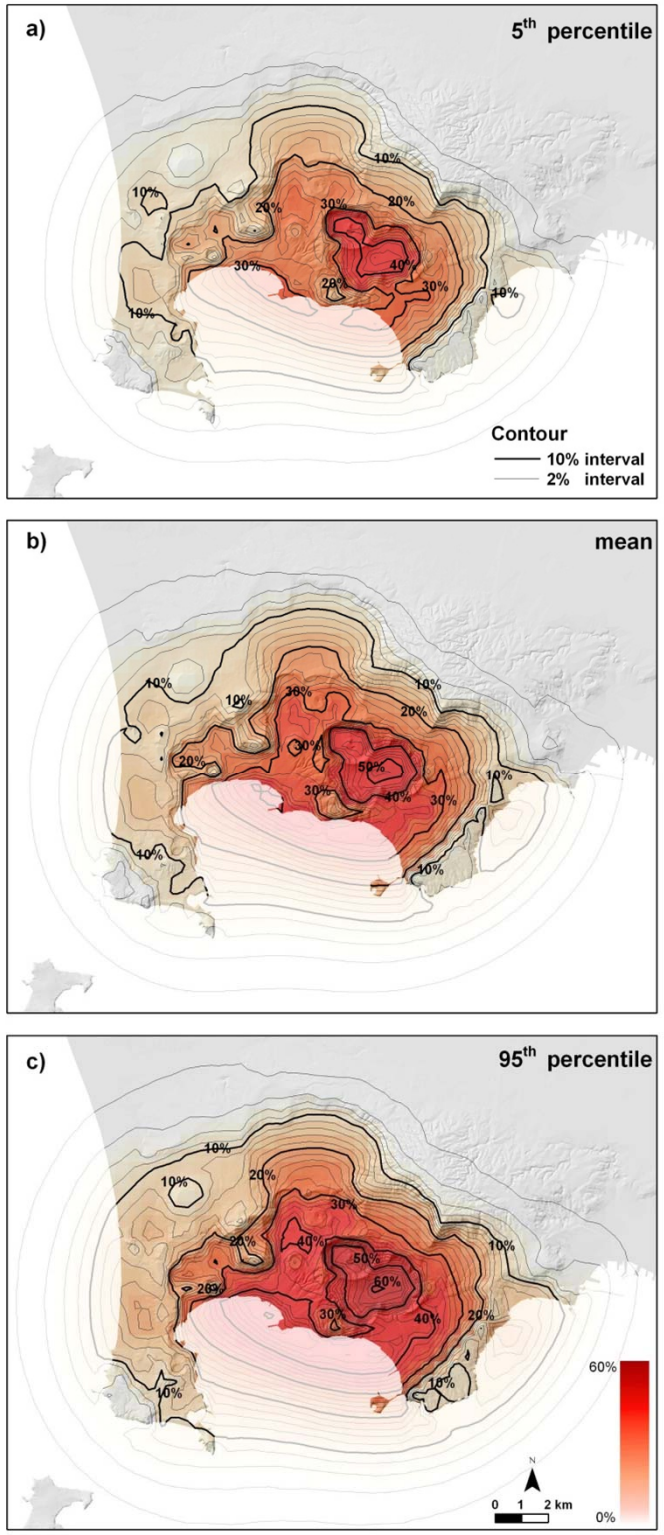

The maps of PDC invasion probability

Combining the spatial probability **map of new vent opening**, the probability distribution of **PDC invasion areas** and by using the **PDC integral box model,** it was possible to produce several probabilistic hazard maps of PDC invasion with their associated uncertainty.

However, **several other maps** were produced to investigate the influence of some key variables or assumptions on the hazard mapping.

All our maps relate solely to the **probability of invasion** by PDCs and not to the distributions of specific hazard variables, such as dynamic pressure, temperature, etc.
It was also assumed that a future PDC episode will originate in the **onland portion** of the caldera because source conditions would be fundamentally and significantly different in the case of an underwater vent.

Figure 13. PDC invasion probability maps computed by assuming the vent opening distribution described in Figure 1 and the spatial density distribution of invasion areas of the last 5 kyr, shown in Figure 3a. The maps assume that PDCs originate from a single vent per eruption, and that the vent is located in the onland part of the caldera. Contours and colours indicate the probability of PDC invasion. The maps relate to: (b) the mean spatial probability, and (a) the 5th and (c) 95th percentiles, respectively.

Conclusions

- The PDC invasion hazard maps produced explicitely consider the **two main unknowns** of the system, i.e. the **vent location** and the **phenomenon scale**, therefore appears to capture the main features of the probability of invasion.

- A primary objective was to **quantify the uncertainty** on the hazard maps and its variability depending on the location; this was produced by using **structured expert judgment** techniques and **Monte Carlo** simulations.

- The analysis may be improved by taking into account **other variables** in the vent opening distribution, **additional data**, and improving the **accuracy of the PDC invasion model**.

- The adopted methodology can be applied to **other volcanic systems and hazards**, and appears to represent a versatile tool to elaborate scientific information for the aim of decision making.